1995ApJ...449..376M

THE ASTROPHYSICAL JOURNAL, 449:376–385, 1995 August 10

EXTREME-ULTRAVIOLET SPECTROSCOPY AND PHOTOMETRY OF EQ PEGASI

BRUNELLA C. MONSIGNORI FOSSI,[1,2] MASSIMO LANDINI,[3] ANTONELLA FRUSCIONE,[2] AND JEAN DUPUIS[2]

Received 1994 December 22; accepted 1995 February 16

ABSTRACT

We present the first spectroscopic extreme-ultraviolet observations of the star EQ Peg (dM4e + dM6e) obtained during a guest observer pointing with the *Extreme Ultraviolet Explorer* (*EUVE*) satellite. EQ Peg was detected in all three spectrometer channels (70–760 Å) and was successfully monitored at the same time by the *EUVE* Deep Survey photometer (67–178 Å). We have identified the main features observed in the spectra and conclude that a number of lines are produced by the highest ionization stages of iron. The detections in the 280–760 Å range are mainly caused by second-order throughput, except for the He II λ304 line. Evidence of activity modulation during the observation is present in both the photometric and spectroscopic data.

Subject headings: line: identification — stars: flare — stars: individual (EQ Pegasi) — ultraviolet: stars

1. INTRODUCTION

EQ Peg (Gl 896AB, BD +19°5116) is a nearby (6.4 pc, 0".155 parallax; Gliese 1969) visual binary system (period ~180 yr, separation 3".7; Kukarkin 1969). Both components of the system are flare stars (Owen et al. 1974; Pettersen 1976) of spectral types dM4e and dM5e (Joy & Abt 1984) and visual apparent magnitudes 10.38 and 12.4, respectively. The brightest component (EQ Peg A) has a stellar radius of 0.38 $R_\odot$, while the companion is somewhat smaller ($R \sim 0.23$ $R_\odot$) (Pettersen, Evans, & Coleman 1984; Bastian 1990). From an activity-rotation relationsip, Doyle (1987) deduced a rotational period of 2.7 days for Gl 896A.

EQ Peg AB has been extensively investigated over a large part of the electromagnetic spectrum, and simultaneous multifrequency observations have been performed. The flare activity is very prominent, and the system exhibits frequent large flares in the *U* band (Lacy, Moffet, & Evans 1976) probably dominated by the fainter star (Baliunas & Raymond 1984). Flare activity in a large number of chromospheric lines, such as Balmer Hα, He I λ5876, sodium D, and ionized calcium infrared triplet lines has been measured (Pettersen et al. 1984) and used to derive constraints on temperature and density conditions in the chromosphere. Monitoring of Hα equivalent width is a well-known diagnostic tool of the chromospheric activity of M dwarfs (Stauffer & Hartmann 1984) and has been systematically applied to the flare detection on EQ Peg (McMillan & Herbst 1991). Ultraviolet observations of the system have been performed by *IUE* (Baliunas & Raymond 1984), and flaring conditions have been detected through the strong enhancement of the emission lines C IV λ1550, C II λ1335, and He II λ1640 and by the increase of the Balmer Hβ line with respect to the continuum. Simultaneous ultraviolet (*IUE*) and X-ray (*EXOSAT*) observations have been reported (Haisch et al. 1987), and *EXOSAT* detected a very large flare during a coordinated X-ray and radio campaign on flare stars (Kundu et al. 1988). The flare emission has been investigated within the framework of the theory of solar two-ribbon flares (Kopp & Poletto 1984), and the very large flair detected by *EXOSAT* has been successfully modeled in detail (Poletto, Pallavicini, & Kopp 1988; Poletto 1989). Microwave (6 and 20 cm) emission of EQ Peg has also been measured by the Very Large Array during quiet conditions and has been attributed to the brighter component (Jackson, Kundu, & White 1989).

EQ Peg was detected as a broadband extreme-ultraviolet (EUV) source during the all-sky survey of both the *ROSAT* Wide Field Camera (Pounds et al. 1993) and the *Extreme Ultraviolet Explorer* (*EUVE*; Bowyer et al. 1994). In this paper we present the first spectroscopic observations of EQ Peg AB obtained in the EUV wavelength range (70–760 Å). The data were collected by the *EUVE* telescope in 1993 August during a guest observer pointing. In § 2 we present the spectroscopic and photometric observations. Section 3 describes the line identifications and the technique used to evaluate the differential emission measure (DEM) distribution and to compute the synthetic spectrum. In § 4 we discuss the activity modulation.

2. OBSERVATIONS AND DATA REDUCTION

2.1. *Spectroscopic Observations*

EQ Peg was observed from 04:41 UT on 1993 August 29 to 11:38 UT on 1993 August 30 during the first year of *EUVE* guest observer pointings. The 20 orbits of continuous observation yielded a total effective exposure time of approximately 40 ks (the spectrometers are shut down during satellite daytime and passage through regions of high particle background such as the South Atlantic Anomaly).

The *EUVE* Deep Survey/Spectrometer (Welsh et al. 1990; Bowyer & Malina 1991) is equipped with a direct broadband imaging detector and three spectrometers to cover the "short" (70–190 Å; SW), "medium" (140–380 Å; MW), and "long" (280–760 Å; LW) EUV wavelengths. The instrument configuration allows simultaneous imaging and spectroscopy, with spectral resolutions of $\Delta\lambda \approx 0.5$, 1, and 2 Å at the short, medium, and long wavelengths, respectively.

Despite the interstellar medium (ISM) attenuation, EUV flux from EQ Peg was detected in all the spectrometer channels, although the long-wavelength detection is mainly the result of second-order throughput. The three spectra were

---

[1] Postal address: Arcetri Astrophysical Observatory, Largo E. Fermi 5, I-50125, Firenze, Italy.

[2] Center for EUV Astrophysics, University of California, Berkeley, 2150 Kittredge Street, Berkeley, CA 94720-5030.

[3] Dipartimento di Astronomia e Fisica dello Spazio, Università di Firenze, Largo E. Fermi 5, I-50125, Firenze, Italy.

extracted from the two-dimensional detector image using the *EUVE* Guest Observer Center software (the IRAF/EUV package) and other standard spectroscopic IRAF tasks.

Particular care was required in performing the subtraction of the background, which dominates the spectra at all wavelengths. The EUV background is predominantly due, in the MW and LW spectrometers, to diffuse emission from interplanetary He II λ304 and He I λ584 photons. A precise background subtraction is therefore particularly important to extract correct information for one of the most interesting stellar emission lines, He II λ304. The optimum extraction was obtained by linearly fitting an average background in two regions of the detector, one from each side of the spectrum. In addition, in order to increase the signal-to-noise ratio (SNR), we restricted the analysis to the "clean" time intervals with the lowest background counts.

Corrections for electronics dead time and limited telemetry allocation (known as "Primbsching") were also applied to the data, resulting in final exposure times of 40,324, 39,539, and 36,533 s for the SW, MW, and LW spectrometers, respectively.

The resulting wavelength-calibrated spectra, corrected with the detectors' effective areas, are illustrated in Figures 1*a*, 2*a*, and 3*a*. The wavelength calibration and instrument effective area were derived from independent in-orbit calibration observations (Boyd et al. 1994).

Figures 1*b*, 2*b*, and 3*b* show the SNR relative to each bin in the extracted spectra. The SNR was computed as

$$\mathrm{SNR}(\lambda) = \frac{S_\lambda}{\sigma(\lambda)} = \frac{S_\lambda}{[S_\lambda + \overline{B}_\lambda(1 + H_{\mathrm{sp}}/H_B)]^{1/2}} ,$$

where $\sigma(\lambda)$ is the standard deviation of the flux measurement, S represents the signal from the target, $\overline{B}$ is the average background subtracted from the total counts, and H_{sp} and H_B are, respectively, the width of the extraction window for the spectrum and for the background in the direction perpendicular to the dispersion.

2.2. *Deep Survey Photometry*

As mentioned in § 2.1, EQ Peg was simultaneously monitored by the Deep Survey (DS) detector. The DS detector is located along the optical axis of the Deep Survey/Spectrometer telescope in the focal plane. It has a field of view approximately 5° in diameter and is divided into a central band for the Lexan/B filter (67–178 Å) and into two sidebands for the Al/C filter (157–364 Å). During a pointed spectroscopic observation, the image of the source forms near the center of the DS detector in the Lexan/B section. The effective area of the DS detector in the Lexan/B filter (e.g., Malina et al. 1994) covers roughly the same wavelength range as the SW spectrometer but peaks

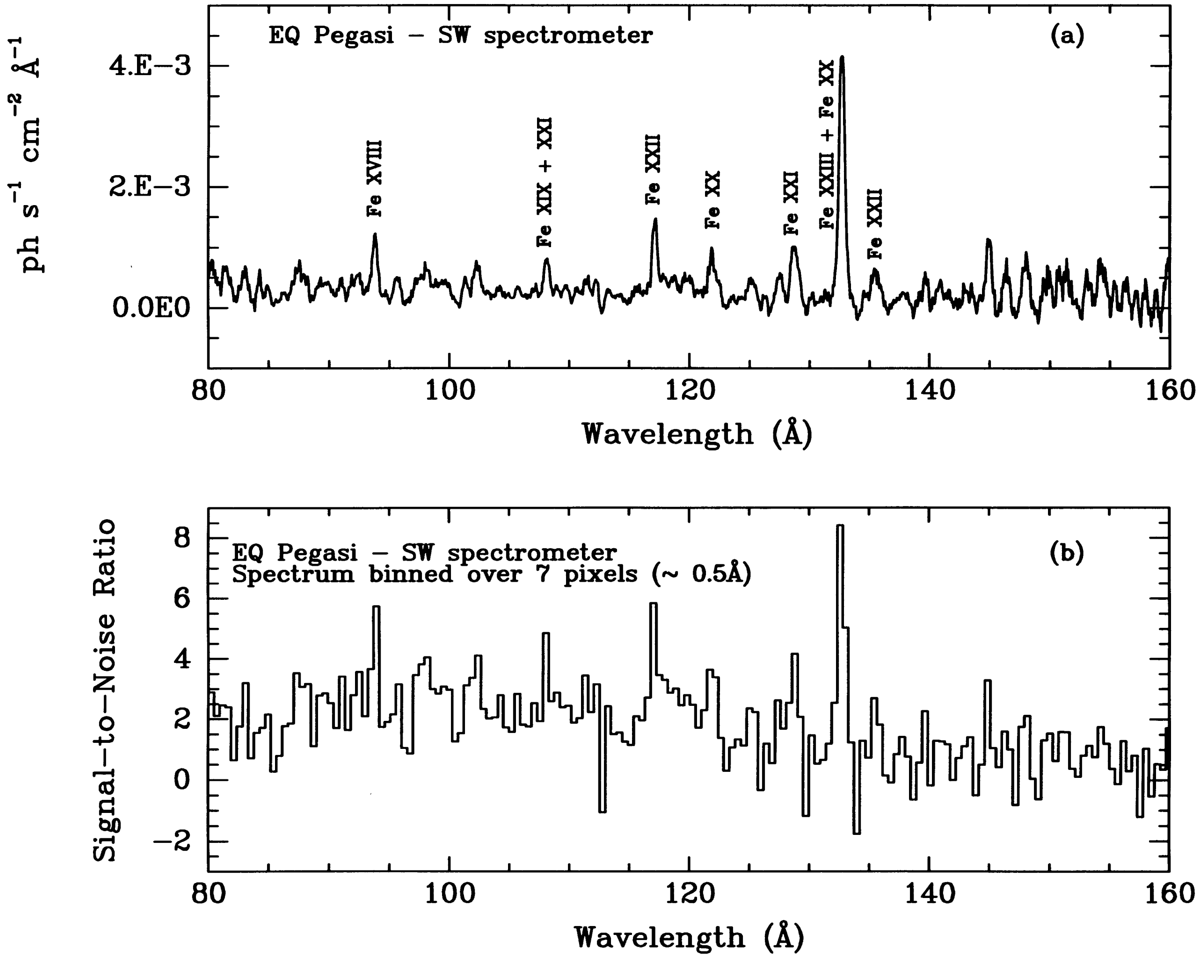

FIG. 1.—(*a*) Flux-calibrated SW EUV spectrum of EQ Peg smoothed over 7 pixels and (*b*) corresponding SNR calculated from the raw count spectrum binned over 7 pixels. Note that the most prominent lines are identified and pertain to the highest ionization stages of iron.

1995ApJ...449..376M

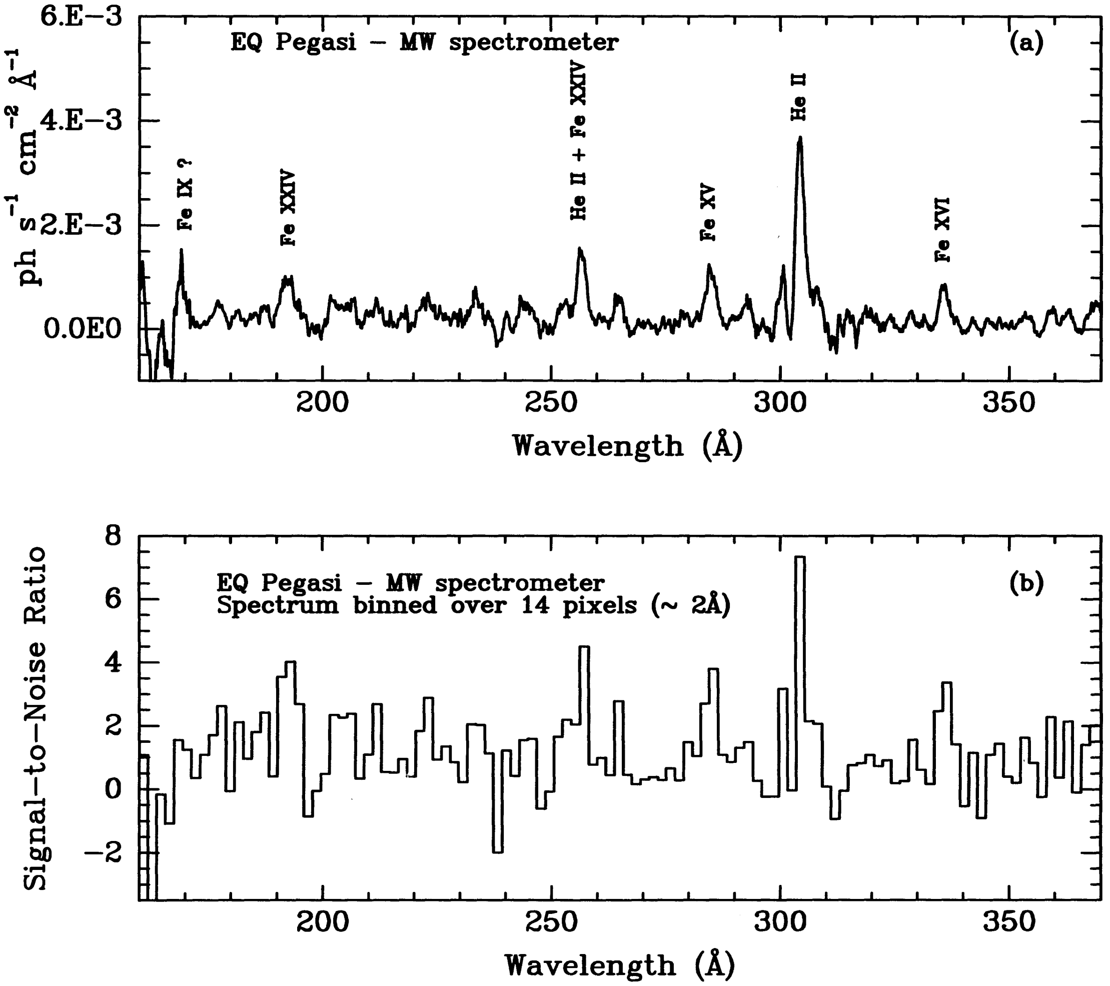

FIG. 2.—Same as Fig. 1, for the MW spectrometer channel with smoothing and binning performed over 14 pixels. In this case the most prominent line pertains to He II; the blend of Fe XII and Fe XXIV is present at ~192 Å.

at ≈ 100 Å with a value about 10 times larger than the SW effective area at peak wavelength. Thus, a proportionally larger count rate results in the DS and allows the generation of a more detailed light curve than from the spectrometer data. For a relatively faint source like EQ Peg, the result is a more reliable monitoring of the EUV variability.

The observation of EQ Peg was obtained after the sensitivity of DS detector had degraded in the boresight vicinity during the observation of the bright white dwarf HZ 43. We have verified that the location of the centroid of the DS image of EQ Peg is indeed very close to the center of the "dead spot." This proximity implies that the absolute value of the flux derived from the nominal DS effective area is incorrect unless a correction factor accounting for the sensitivity loss is applied. We have estimated this correction factor by taking the ratio of the mean count rate during the second nighttime pass to that of the following consecutive six nighttime passes. This correction factor is approximately 2 and is likely to be uncertain up to 15%–25% according to Sirk (1994). We were also concerned about the probable apparition of spurious features in the light curve because of small spacecraft motions that could take the DS image of EQ Peg outside of the dead spot where the detector sensitivity is maximal. With the exception of the first two orbits, where the image of the source was found to extend out of the dead spot (see the DS light curve in Fig. 4), we have explicitly verified that for the remainder of the observation, the source was located within the dead spot. The flares detected during the second half of the observation are not artifacts of the dead spot since the DS photometry is valid in a relative sense. Indeed, a comparison between light curves of the SW (Fig. 4*a*) and the DS (Fig. 4*b*) detectors clearly shows the correlation between the flares.

The DS data were processed and analyzed using the software provided by the *EUVE* Guest Observer Center. Part of the software can be applied to the DS data to produce DS QPOE files in the same manner as for spectrometer data. For the light-curve generation, we have used the XTIMING (within XRAY) package available in IRAF. As the source region we selected a circle centered on EQ Peg with a radius large enough to include all the source photons (about 2.′8). The region selected for the background was a circle about 11′ away from the source with a radius of 4.′5. Light curves for EQ Peg were generated using the task LTCURV that automatically applies the background subtraction and effective time calculation for each time bin. A similar procedure was applied to get the light curves for individual emission lines (see § 4).

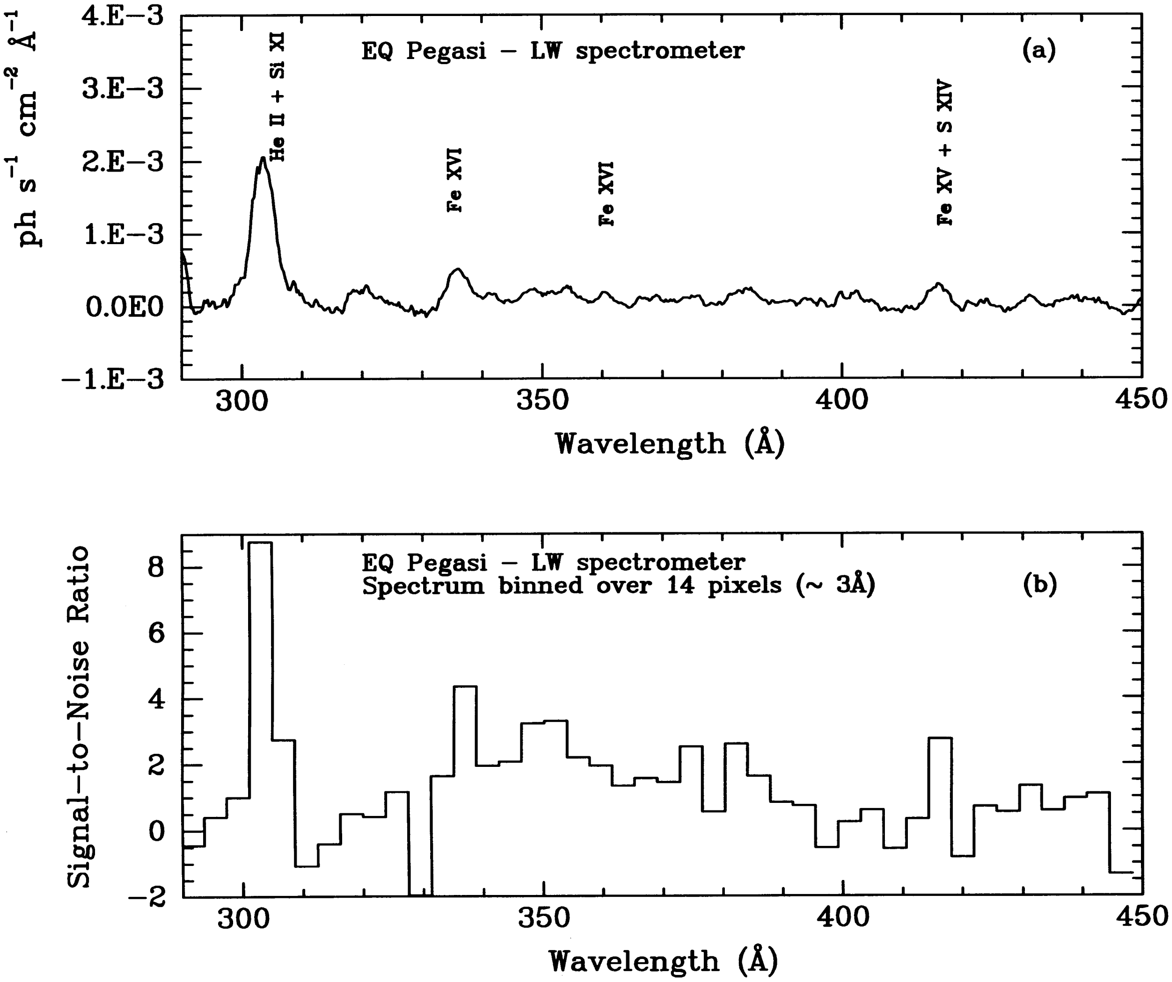

FIG. 3.—Same as Fig. 1, for the LW spectrometer channel. The most prominent lines pertain to He II and the Na-like doublet of Fe XVI. Note that the signal above 440 Å is dominated by second-order contributions.

Figure 4*a* is the DS Lexan/B light curve of EQ Peg in 500 s time bins, and Figure 4*b* is the corresponding SW channel light curve in 600 s time bins. The data *consistently* indicate that two flares occurred during the second half of the observation. In Figures 5 and 6, we show an enlargement of the two time intervals when the flares were observed with a higher (100 s) time resolution.

We estimated the total flux emitted during the entire DS observation from the measured count rate. We used the Monsignori Fossi & Landini (1994a) spectral code for a temperature of 6×10^6 K for the quiescent phase, $\simeq 10^7$ K for the first flare peak, and $\simeq 2 \times 10^7$ K for the second large flare peak. We assumed $N_{\rm H} = 1.4 \times 10^{18}$ cm^{-2} (see § 3.1 below). We derived a luminosity of 1.15×10^{28} ergs s^{-1} for the quiescent period, 7.0×10^{28} ergs s^{-1} for the first peak, and 1.15×10^{29} ergs s^{-1} at the second peak. The luminosity measured during the quiescent period is in good agreement with the luminosity derived from the count rate measured in the Lexan/B band during the *EUVE* all-sky survey (0.11 counts s^{-1}).

The large AU Mic flare observed in 1992 July 15 (Cully et al. 1994) reached a peak luminosity of 10^{30} ergs s^{-1} and a total energy of 3×10^{34} ergs. In comparison, we estimate a total energy of 1.7×10^{33} ergs for the two flares on EQ Peg, i.e., about 20 times weaker than the large AU Mic flare.

3. SYNTHETIC SPECTRA

3.1. *Line Intensity*

Several bright lines, which can be identified through comparison with solar and laboratory spectra, are visible in Figures 1*a*, 2*a*, and 3*a*. From the intensity of these lines (see paragraph below) it is possible to evaluate the DEM as a function of temperature, to simulate the theoretical spectrum emitted by the source, and to perform further identifications of minor features.

The intensity of a spectral line ($i \rightarrow j$) for an optically thin coronal plasma is given by

$$\begin{aligned} I_{ij} &= K\ \mathrm{Ab(Z)} e^{-\sigma(\lambda) N_{\rm H}} \int_V G_{ij}(T, N_e) N_e^2\, dV \\ &= K\ \mathrm{Ab(Z)} e^{-\sigma(\lambda) N_{\rm H}} \int_T G_{ij}(T, N_e) f(T) dT \ \text{photons cm}^{-2}\ \text{s}^{-1}, \end{aligned} \tag{1}$$

where K is a constant that takes into account the properties of the instruments and the star distance; Ab(Z) is the abundance of element Z relative to H; $f(T) = N_e^2(dV/dT)$ is the differential emission measure, i.e., a measure of the amount of emitting

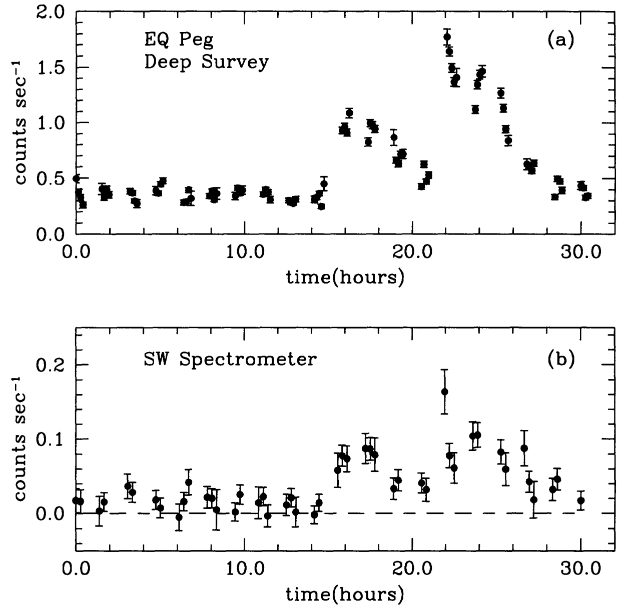

FIG. 4.—(*a*) Light curve obtained from the DS photometer data and (*b*) corresponding light curve obtained from the SW spectrometer data. The time bins are 500 and 600 s for the DS photometer and the SW spectrometer, respectively. The start time corresponds to 04:54:28 UT on 1993 August 29.

material in the temperature interval from T to $T + dT$; $N_{\rm H} = \int n_{\rm H} dh$ is the hydrogen column density to the star; $\sigma(\lambda)$ is the ISM absorption cross section; and $G_{ij}(T, N_e)$ (the contribution function) is the power emitted per unit emission measure and is a function of the atomic line data, which is related to the electron temperature (T) mainly through the ion abundance and to the electron density (N_e) mainly through the level population.

To evaluate the contribution functions $G_{ij}(T, N_e)$, we have used an updated version of the spectral emission code developed by Landini & Monsignori Fossi (1990) and Monsignori Fossi & Landini (1994a). We adopted the ISM photoionization cross sections of Rumph, Bowyer, & Vennes (1994), which include the neutral He autoionization features

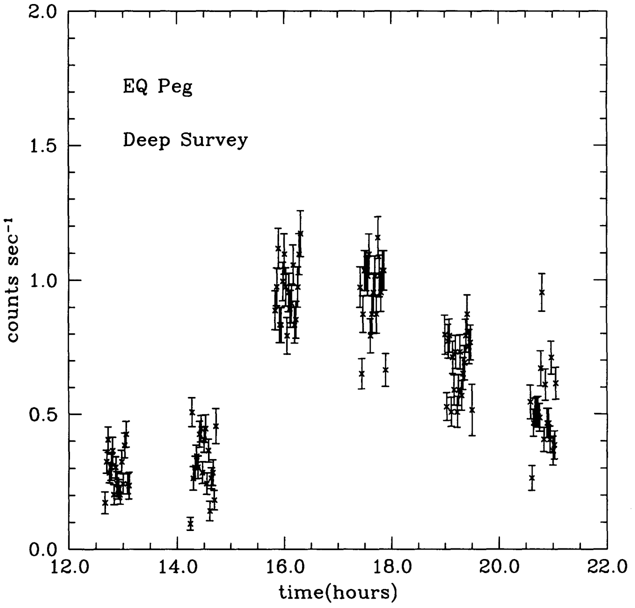

FIG. 5.—DS light curve for the first flare (time resolution 100 s)

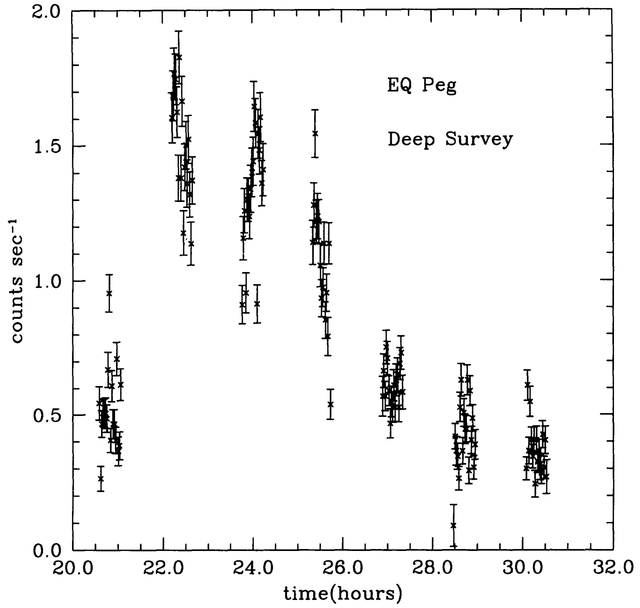

FIG. 6.—DS light curve for the second flare (time resolution 100 s)

To our knowledge, no direct measurement exists of the hydrogen column density N(H I) in the direction of EQ Peg. Therefore, we estimated N(H I) = 1.34 × 10^{18} cm^{-2} from a mean interstellar hydrogen density of 0.07 cm^{-3} (Paresce 1984) and a distance of 6.4 pc (Gliese 1969). We compared this value with the best estimate from a new physical model of the ISM (Jelinsky & Fruscione 1995) that employs a three-dimensional interpolation method on a large database of hydrogen column densities (Fruscione et al. 1994, plus additional data). The model gives a best-fit value of N(H I) = 3.31 × 10^{18} cm^{-2}, i.e., a factor of 2.5 higher. However, since only a few direct measurements of N(H I) are present in the database at such nearby distances, the typical error in the model is about 0.3–0.4 dex at the distance of EQ Peg; therefore, the estimates are compatible within the errors. We assumed N(H I) = 1.34 × 10^{18} cm^{-2} throughout the paper.

In order to obtain information on the distribution of emitting material as a function of temperature, we derived a model of the DEM model $f(T)$ by combining the measurements of the fluxes for a set of spectral lines with the knowledge of the appropriate contribution functions G_{ij}. The numerical procedure that we used to fit the DEM distribution function $f(T)$ minimizes the square of the differences between observed and predicted fluxes of the selected lines (see Monsignori Fossi & Landini 1991a, b, 1994b for further details on the method).

3.2. *Differential Emission Measure and Line Identification*

We have marked in Figures 1*a* and 1*b* all emission features with SNR ≥ 3 that we have identified in the SW and MW spectra. We have used all these lines (except for the He II + Fe XXIV blend) plus an upper limit for the Fe IX λ171 line to perform the DEM analysis. Using the spectral code of Monsignori Fossi & Landini (1994a), we have evaluated the power emitted per unit emission measure for each selected wavelength

1995ApJ...449..376M

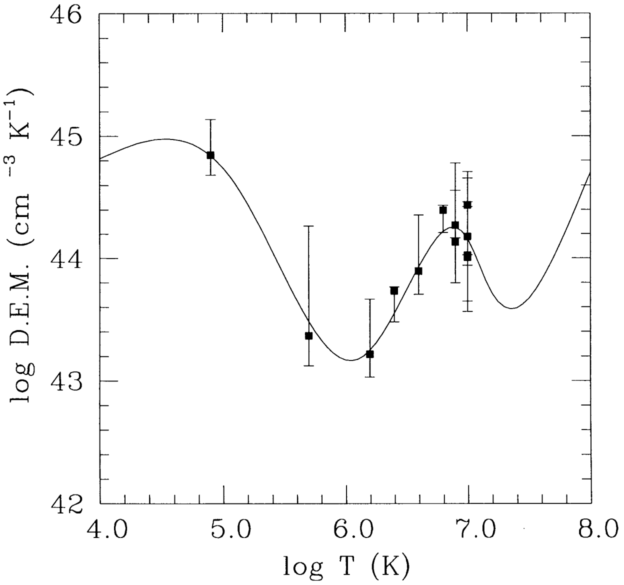

FIG. 7.—DEM distribution that best fits the *EUVE* spectroscopic observations of EQ Peg. Squares refer to the observations and are plotted for the temperature at which the product $G(T) \times \mathrm{DEM}(T)$ reaches the maximum value. The error bars on the observations indicate the uncertainties of the DEM. The minimum at $\approx 10^6$ K is mainly due to the presence of the upper limit for the Fe ix line among the features selected for the fit. The increase in the DEM distribution for temperatures larger than 3×10^7 K is not well constrained since no EUV spectral features can be ascribed to temperatures larger than 2×10^7 K. The high-temperature continuum is not detected in the SW spectrum.

bin including both line and continuum contributions for an electron density of 10^{13} cm^{-3}. Figure 7 shows the volume DEM distribution that best reproduces the observations within the observed errors. Uncertainties in the DEM distribution are indicated by the error bars of the observations plotted for the temperature at which the product $G(T) \times \mathrm{DEM}(T)$ reaches its maximum value.

The selected lines allowed us to perform a rather detailed diagnostic of the emitting plasma in the temperature interval between $\log T = 5.8$ and $\log T = 7.2$. Little information exists for the low-temperature regime, which is constrained only by the He ii Lyα line. However, this line is probably optically thick and can give only a lower limit for the DEM distribution at $\approx 10^5$ K. A high-temperature ($\log T \geq 7.5$) component appears to be necessary to get a good fit for the Fe xxiv λ192.03 line.

The DEM distribution shows a minimum at $\approx 10^6$ K, mainly due to the presence of the upper limit for the Fe ix line among the features selected for the fit. A well-constrained maximum is visible at $10^{6.8}$ K. The observed increase in the DEM distribution for temperatures larger than 3×10^7 K is not well constrained since no EUV spectral features (except for the Fe xxiv + Fe xii λ192 blend) can be ascribed to temperatures larger than 2×10^7 K. The continuum in the SW spectrum could give information on the high-temperature DEM distribution, but it is not detected above the background noise. Therefore, the DEM distribution for temperatures greater than 10^7 K is highly insensitive to the *EUVE* data.

Figure 8 illustrates the results of the fitting procedure: Figure 8*a* plots the observed versus predicted fluxes (a few lines are not properly reproduced within the errors; e.g., Fe xviii λ93.8). The *quality ratio*, $I_{\mathrm{obs}}/I_{\mathrm{pred}}$, is plotted for each bin as a function of wavelength (Fig. 8*b*), of the temperature of the maximum value of the contribution function (Fig. 8*c*), and of the temperature of the maximum value of the product $G(T) \times f(T)$ (Fig. 8*d*).

We used the best-fit DEM distribution to evaluate the synthetic spectrum in the wavelength region of interest and to analyze the contribution of different lines to the selected bins. Figures 9*a* and 9*b* reproduce the synthetic spectra convolved with the instrument point-spread function smoothed similarly to the observed spectra (Figs. 1*a* and 2*b*) for the SW and MW ranges.

A detailed comparison between the predicted and the observed spectra allows the identification of several minor emission lines. In Table 1 we list the observed and the theoretical wavelengths (Monsignori Fossi & Landini 1994) for all the identified lines (non–density sensitive) of the ions that contribute to the bin selected for the DEM analysis.

The large feature at ≈ 256 Å is probably a blend of Fe xxiv λ256.10 and He ii λ256.30, but we cannot correctly reproduce the observed flux. The Fe xviii λ93.80 line presents a few problems: the observed flux is not well reproduced and it is not consistent with the flux of the λ103.94 line of the same ion, which should have about half of the flux.

Three density-sensitive lines of Fe xxi fall within the SW spectral range. Fe xxi λ128.73 and λ102.22 are both detected with SNR ≥ 3; the faint feature observed at 144.9 Å could be

TABLE 1

LINE IDENTIFICATION

Ion	λ_{obs} (Å)	λ_{theo} (Å)	$F_{\mathrm{obs}} \times 10^{-4}$ (photons cm^{-2} s^{-1} Å^{-1})	$F_{\mathrm{pred}} \times 10^{-4}$ (photons cm^{-2} s^{-1} Å^{-1})
Fe xviii	93.80	93.93	5.4 ± 0.9	4.0
Fe xxi	98.02	97.88	2.9 ± 1.8	1.1
Fe xix + xxi	108.17	108.37	3.9 ± 0.8	4.2
Fe xxii	117.16	117.18	6.5 ± 3.2	3.7
Fe xx	118.69	118.66	2.1 ± 0.7	2.9
Fe xx	121.91	121.63	3.5 ± 1.2	4.6
Fe xxiii + xx......	132.73	132.84 + 132.86	20.0 ± 2.2	21.0
Fe xxii	135.47	135.76	3.5 ± 1.2	5.0
Fe ix	169.90	171.07	≤ 7.0	10.0
Fe xxiv	192.32	192.03	14.0 ± 4.2	14.0
Fe xv	284.74	284.15	22.0 ± 7.0	15.0
He ii	304.10	303.78	110.0 ± 16	110.0
Fe xvi	335.67	335.41	27.0 ± 8.2	29.0
Fe xvi	359.58	360.11	≤ 16.0	16.0

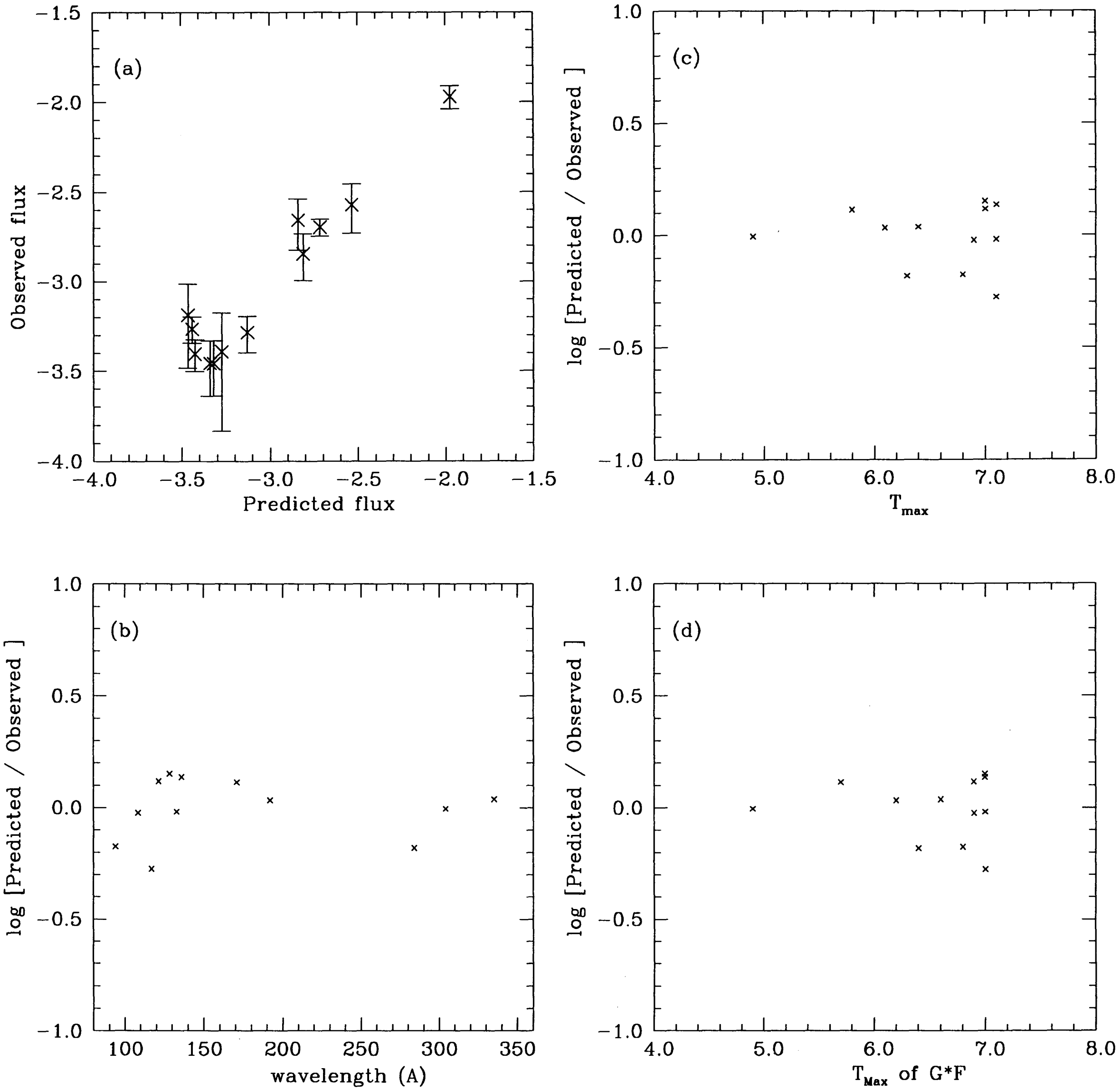

FIG. 8.—Results of the fitting procedure: (*a*) observed vs. predicted fluxes, (*b*) quality factor ($I_{\rm obs}/I_{\rm pred}$) vs. wavelength, (*c*) temperature of the maximum value of the contribution functions, and (*d*) temperature of the maximum value of the product $G(T) \times f(T)$.

identified with the Fe XXI λ145.65 line, but the wavelength shift seems too large. Using the density-sensitive ratio (Fe XXI λ128.73/Fe XXI λ102.22), we estimate an electron density of $\simeq 10^{13}$ cm^{-3}, in agreement with the assumption of the model. This density value is also consistent with the intensity of the feature at 108.17 Å that should be mainly caused by Fe XIX λ108.37 with 10% contribution of Fe XXI λ108.45.

4. ACTIVITY MODULATION IN THE LINES

The count rate of a few very bright lines was high enough to study the time evolution of the emission and to investigate the modulation from either flare activity or the appearance of active regions. The light curves of the brighter lines have been obtained using the XTIMING software in the IRAF/XRAY package. The count rate was integrated over 2000 s time bins, and the resulting light curves are shown in Figures 10*a* and 10*b* for the Fe XVIII λ94 and the Fe XVIII λ133 lines of the SW spectrum and in Figures 11*a* and 11*b* for the Fe XXIV λ192 and the He II λ304 lines of the MW spectrum. Activity modulation is clearly visible in the case of the Fe XVIII line, and the general behavior is, in all cases, in good agreement with the DS observation.

5. SUMMARY

Despite the relatively short exposure time (≈40 ks), EQ Peg was significantly detected over the entire EUV wavelength range. Several emission lines corresponding to the highest ionization stages of iron (from Fe XVIII to Fe XX) have been identified in the SW spectrum; He II, Fe XXIV, Fe XV, and Fe XVI lines are present in the MW spectrum; while the He II Lyα line (the most prominent feature) and the Fe XVI λ335.4 line are identified in the LW spectrum. The SNR is too low to clearly identify the other component of the Na-like doublet of Fe XVI λ360.8 in the LW spectrum.

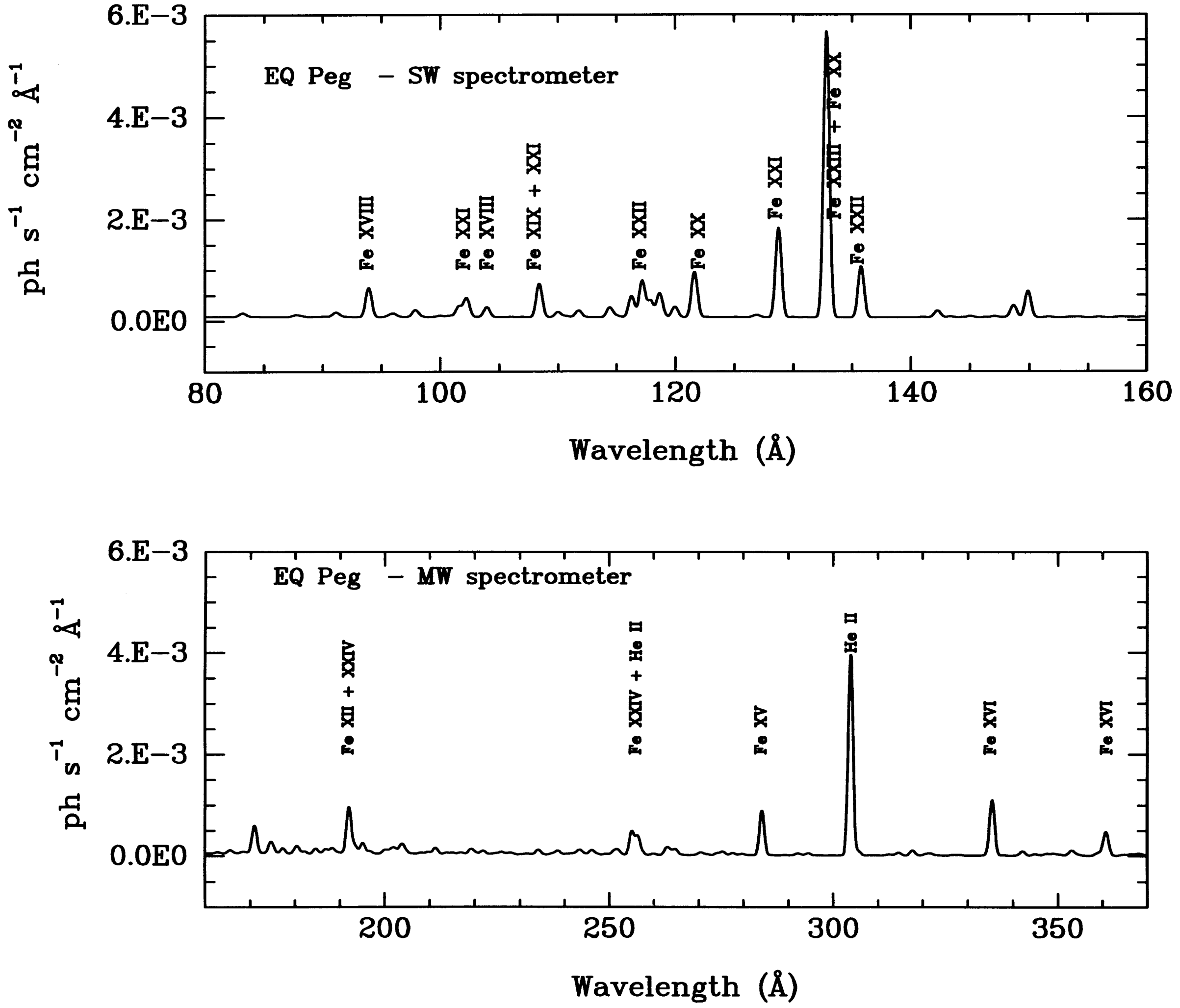

FIG. 9.—EUV synthetic spectra for (*a*) the SW and (*b*) the MW spectral ranges; the spectra have been convolved with the instrument point-spread function

A longer exposure time could not only provide more information about the Fe XVI λ360.8 line but also clarify whether the feature at ~417.2 Å can be ascribed to a blend of Fe XV and S XIV. Furthermore, a good detection of the Na-like iron lines would allow a comparison of the observed to the predicted ratio, putting strong constraints on the unknown amount of hydrogen absorption in the direction of EQ Peg.

The DEM distribution shows a minimum at 10^6 K and a bump at $\approx 6 \times 10^6$ K. A hotter tail in the DEM distribution is needed to reproduce the intensity of the Fe XXIV λ192 line. However, it should be noticed that such high temperature could be due to the presence of two strong flares during the observation: an analysis of the DEM distribution during the flares seems to indicate the presence of hotter plasma at temperatures greater than 10^7 K.

The emission measure distribution derived from the *EUVE* spectrum of Capella by Dupree et al. (1993) also shows a minimum at $\approx 10^6$ K and a maximum at $\approx 6 \times 10^6$ K; but for temperatures larger than 10^7 K, the tail in Capella's DEM seems well constrained by the presence of the continuum in the short-wavelength spectrum. To explain the high-temperature tail, Dupree et al. (1993) present several plausible hypotheses. In the SW spectrum of EQ Peg, the continuum is not clearly detected and the high-temperature tail could only be ascribed to the presence of the two flares during the observation.

An activity modulation over timescales of several minutes was observed on the DS photometer and on the SW channel light curves. The light curve of the Fe XXIII line seems in rather good agreement with the DS data. The time modulation of the Fe XXIII, Fe XVIII, and He II lines deserves more attention and elaboration in order to compare it with similar events already observed on many flare stars and the Sun and in order to have better insight into the modeling of solar-type stellar activity. Work is in progress to study the activity modulation.

We wish to thank Jeremy J. Drake and Mihalis Mathioudakis for the useful discussions. B. C. M. F. wishes to thank Stuart Bowyer, Roger F. Malina, and the *EUVE* science team for the warm hospitality during her stay at the Center for EUV Astrophysics. We are grateful to the CEA editorial team for help in preparing the manuscript. This work has been supported by the Italian Space Agency (ASI) and NASA contract NAS5-30180.

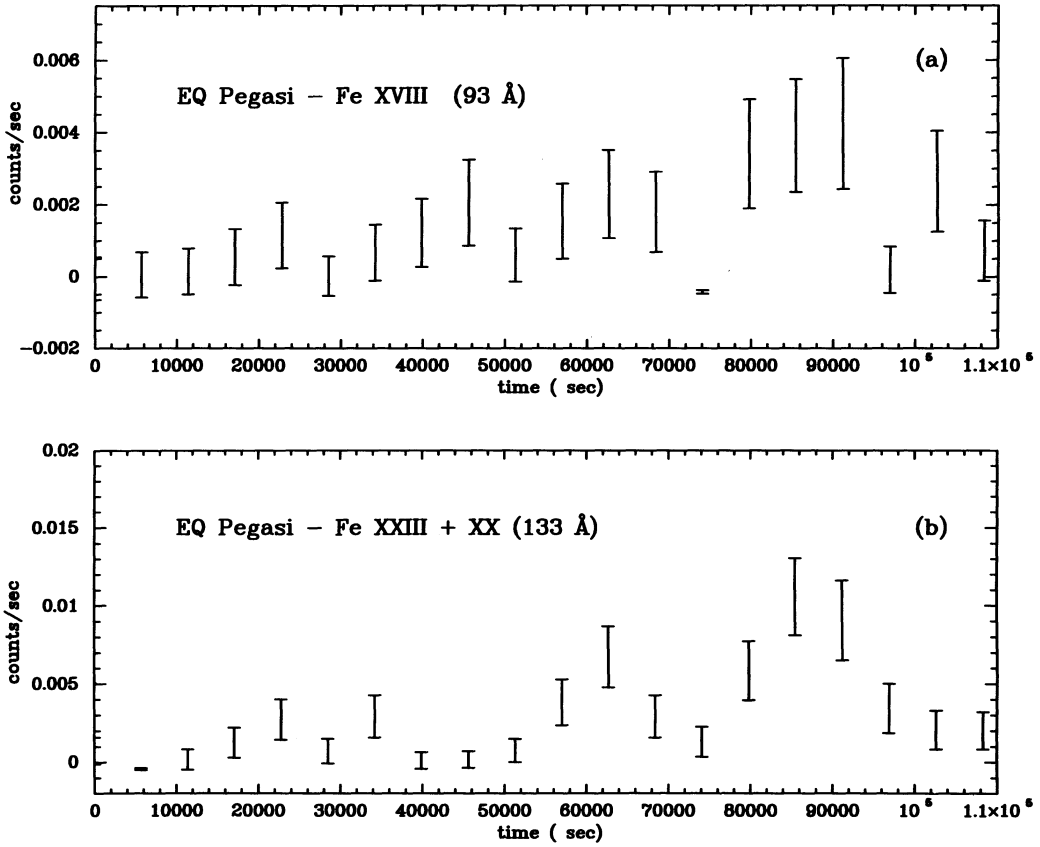

FIG. 10.—Light curves for (*a*) the Fe XVIII λ93 and (*b*) the Fe XXIII + Fe XX λ133 lines in the SW spectrum

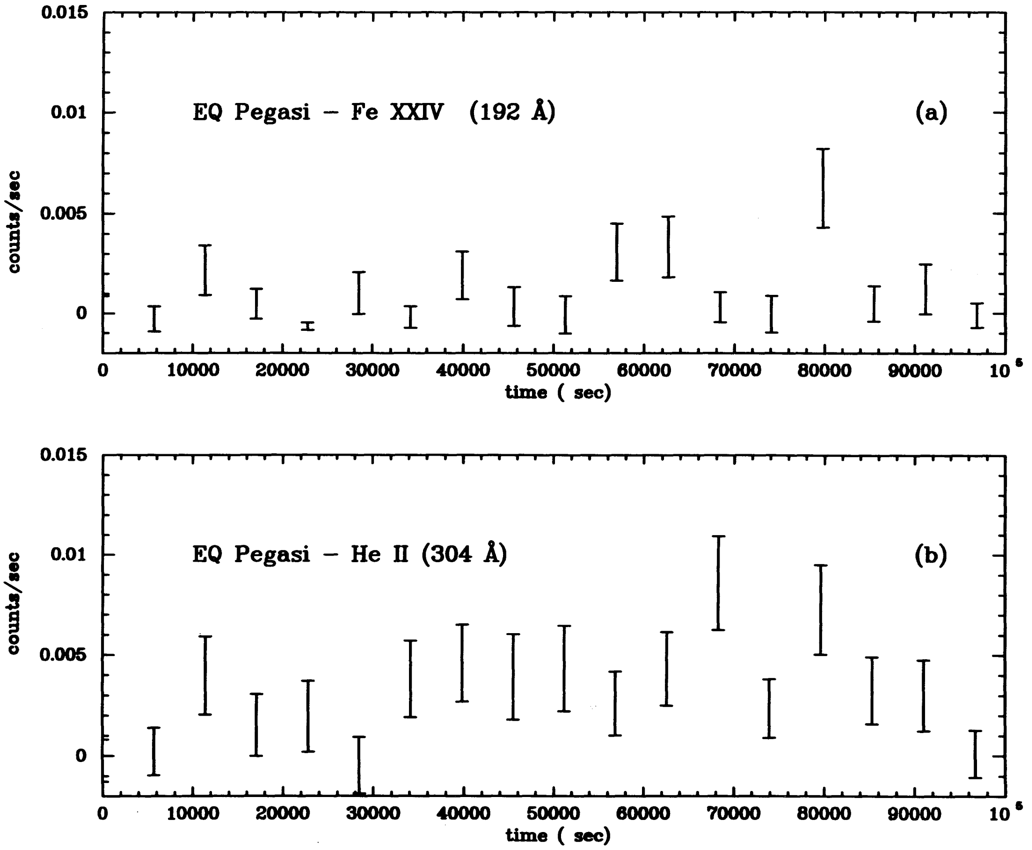

FIG. 11.—Light curve for (*a*) the Fe XXIV λ192 and (*b*) the He II λ304 lines in the MW spectrum

REFERENCES

Baliunas, S. L., & Raymond, J. C. 1984, ApJ, 282, 728

Bastian, T. S. 1990, Solar Phys., 130, 265

Bowyer, S., Lieu, R., Lampton, M., Lewis, J., Wu, X., Drake, J. J., & Malina, R. F. 1994, ApJS, 93, 569

Bowyer, S., & Malina, R. F. 1991, in Extreme Ultraviolet Astronomy, ed. R. F. Malina & S. Bowyer (New York: Pergamon), 397

Boyd, W., Jelinsky, P., Finley, D. S., Dupuis, J., Abbott, M., Christian, C., & Malina, R. F. 1994, Proc. SPIE, 2280, 280

Cully, S., Fisher, G. H., Abbott, M. J., & Siegmund, O. H. W. 1994, ApJ, 435, 449

Doyle, J. G. 1987, MNRAS, 224, 1

Dupree, A. K., Brickhouse, N. S., Doscheck, G. A., Green, J. C., & Raymond, J. C. 1993, ApJ, 418, L41

Fruscione, A., Hawkins, I., Jelinsky, P., & Wiercigroch, A. 1994, ApJS, 94, 127

Gliese, W. 1969, Catalogue of Nearby Stars (Veröff. Astron. Rechen-Inst. Heidelberg, 22)

Haish, B. M., Butler, C. J., Doyle, J. G., & Rodono, M. 1987, A&A, 181, 96

Jackson, P. D., Kundu, M. R., & White, S. M. 1989, A&A, 210, 284

Jelinsky, P., & Fruscione, A. 1995, in preparation

Joy, A. H., & Abt, H. A. 1984, ApJS, 28, 7

Kopp, R. A., & Poletto, G. 1984, Solar Phys., 93, 351

Kukarkin, B. V. 1969, General Catalogue of Variable Stars (Moscow: Sternberg Astron. Inst.)

Kundu, M. R., Pallavicini, R., White, S. M., & Jackson, P. D. 1988, A&A, 195, 159

Lacy, C. H., Moffet, T. J., & Evans, D. S. 1976, ApJS, 30, 85

Landini, M., & Monsignori Fossi, B. C. 1990, A&AS, 91, 183

Malina, R. F., et al. 1994, AJ, 107, 751

McMillan, J. D., & Herbst, W. 1991, AJ, 101, 1789

Monsignori Fossi, B. C., & Landini, M. 1994a, Solar Phys., 152, 81

———. 1991a, Adv. Space Res., 11, 281

———. 1991b, in Intensity Integral Inversion Techniques, ed. R. A. Harrison & A. M. Thompson, RAL-91-092, 27

———. 1994b, A&A, 284, 900

Owen, F. N., Bopp, B. W., Moffet, T. J., & Laxor, J. F. 1974, ApJ, 10, L37

Paresce, F. 1984, ApJ, 89, 1022

Pettersen, B. R. 1976, Inst. Theor. Astrophys. Blinderen—Oslo, Rep. 46

Pettersen, B. R., Evans, D. S., & Coleman, L. A. 1984, ApJ, 282, 214

Poletto, G. 1989, Solar Phys., 121, 313

Poletto, G., Pallavicini, R., & Kopp, R. A. 1988, A&A, 201, 93

Pounds, K. A., et al. 1993, MNRAS, 260, 77

Rumph, T., Bowyer, S., & Vennes, S. 1994, AJ, 107, 2108

Sirk, M. 1994, EUVE internal memo 0084/94

Stauffer, J. R., & Hartmann, L. W. 1984, ApJS, 61, 531

Welsh, B. Y., Vallerga, J. V., Jelinsky, P., Vedder, P. W., & Bowyer, S. 1990, Opt. Eng., 29, 752